J Appl Electrochem (2010) 40:581–592
DOI 10.1007/s10800-009-0033-x

ORIGINAL PAPER

New oxygen evolution anodes for metal electrowinning: investigation of local physicochemical processes on composite electrodes with conductive atomic force microscopy and scanning electrochemical microscopy

Sönke Schmachtel · Sascha E. Pust · Kyösti Kontturi · Olof Forsén · Gunther Wittstock

Received: 10 March 2009 / Accepted: 23 November 2009 / Published online: 18 December 2009

Abstract Atomic force microscopy (AFM), conductive atomic force microscopy (CAFM) in air, and scanning electrochemcial microscopy (SECM) in 2 M H_2SO_4 have been used to investigate model composite electrodes obtained by pressing sieved MnO_2 particles into a Pb matrix. These model electrodes shall resemble new composite electrodes produced by coldspraying and currently being tested for Zn electrowinning. CAFM showed a very uneven distribution of the current path through the matrix electrode with the highest currents measured at the MnO_2/Pb domain boundary. SECM images in the substrate-generation/tip-collection mode in vertical and horizontal planes could show spatial concentration distribution of H^+, O_2 and H_2O_2 that could be evaluated qualitatively despite interfering turbulent convection due to raising gas bubbles. There is a concentration overvoltage due to deviations of the H^+ and O_2 concentration close to the surface from the bulk value. It amounts to about 40–50 mV for both compounds. H_2O_2 is formed as an intermediate and is consumed at the MnO_2 catalyst particles.

Keywords Composite electrodes · Electrowinning · Lead electrode · Manganese dioxide · Electrocatalysis · Oxygen evolution · Atomic force microscopy · Conductive atomic force microscopy · Scanning electrochemical microscopy

S. Schmachtel · K. Kontturi (✉)
Laboratory of Physical Chemistry and Electrochemistry, Helsinki University of Technology (TKK), P.O. Box 6100, 02015 Espoo, Finland
e-mail: kontturi@cc.hut.fi

S. Schmachtel · O. Forsén
Laboratory of Materials Chemistry and Corrosion, Helsinki University of Technology (TKK), P.O. Box 6200, 02015 Espoo, Finland

S. E. Pust · G. Wittstock (✉)
Department of Pure and Applied Chemistry, Carl von Ossietzky University of Oldenburg, Faculty of Mathematics and Science, Center of Interface Science (CIS), 26111 Oldenburg, Germany
e-mail: gunther.wittstock@uni-oldenburg.de

Present Address:
S. E. Pust
IEF5 – Photovoltaik, Forschungszentrum Jülich GmbH, 52425 Jülich, Germany

1 Introduction

The most common electrochemically won and refined metals are Zn and Cu. Ni and Co, but also Cd, Mn, Sn and Cr can be produced electrochemically. Oxygen evolution is a common counter reaction for metal electrowinning. In most cases the electrolytes are sulfuric acid solutions of different concentration [1], where the main reaction is the water oxidation reaction which produces oxygen and acid:

$$2H_2O_{(l)} \rightarrow O_{2(g)} + 4H^+_{(aq)} + 4e^- \quad (1)$$

Unfortunately this reaction is generally connected to a very high oxygen evolution overpotential η_{O_2}. For instance, in Zn electrowinning it accounts for about 800 mV or 20–25% of the total electrical energy [1]. In Cu electrowinning, a decrease of the operation potential can be achieved by the addition of Co^{2+} ions to the solution which efficiently depolarize the anode [1]. However, this possibility does not exist for Zn electrowinning, because cations of the elements like Ni, Co, Sb, Sn catalyze the hydrogen evolution or cause the re-dissolution of Zn from the cathodes [1].

The dimensionally stable anode (DSA^{TM}) technology also known as the coated Ti anode (CTA) [2] which has its

origins in the chlor-alkali industry [3–12] has been suggested for the decrease of the operation potential. Apart from a few special applications [13–15], it is not being used in metal electrowinning. The main drawback of DSA remains its high investment cost, which are due to the high prices of titanium substrates, precious metals, and the coating procedure. A typical plant often comprises over 10000 anodes leading to requiring very high investment for the introduction of DSA technology. This is in contrast to the chlor-alkali process with higher current densities and lower electrode areas making it very challenging for DSA to compete economically with the traditional Pb anode systems in electrowinning [2].

In view of this situation we aim for new production routes for DSA-analogue electrodes based on more economically electrocatalysts and production methods. Additionally, the new technology should be easy to integrate into existing tank house structures. Our approach follows earlier developments by Outotec to apply a catalytically active coating onto existing Pb anodes by a spraying method [16, 17]. Patented processes in this context are high velocity oxygen fuel (HVOF) spraying and cold spraying [18]. Cold spraying has been shown to be superior to HVOF, because it is a low temperature method which does not affect the composition and modification of the catalyst.

In order to facilitate the catalyst development, an ex situ method was used for testing MnO_2 catalysts pressed together with a Pb support into tablet composite electrodes [19]. The composite electrodes resemble sprayed coatings, because in the spraying process the catalyst is shot/buried into the soft Pb matrix material and gives a composite coating on top of the standard Pb-based anode [16]. In this respect composite electrodes can be considered to be a model system for the sprayed coatings produced for industrial purposes.

The first results from rotating disc electrode (RDE) measurements with composite anodes showed that the achieved current densities j for O_2 evolution were dependent on the rotation rate [20]. Further tests using vertically oriented MnO_2–Pb composite electrodes confirmed a considerable improvement compared to the commonly used Pb anode alloyed with (0.5–1)% Ag (PbAg) [19]. It was also shown that j was inversely proportional to the mean MnO_2 particle size r ($j \propto 1/r$).

A similar relation was derived in the same paper [19], assuming that the oxygen evolution process occurs only close to the catalyst-matrix-electrolyte three-phase boundary line. The statistical treatment of cuts through a matrix with randomly arranged spherical particles resulted in the following expression for the overall current passing through the composite electrode:

$$i = 0.75\pi nFBk\frac{A_{\text{geom}}w}{r} \tag{2}$$

where F is the Faraday constant, n is the number of electrons transferred per molecule, B is a proportionality constant dependent for instance on the active sites per boundary length unit, k is an electrochemical rate constant, A_{geom} is the geometric area of the entire composite electrode and w is the ratio of MnO_2 volume to total volume of the composite and r is the radius of the catalyst particles used in the composite.

We identified four different processes, that could force the current through a region along the three phase boundary line [19]: (i) MnO_2 has a much higher electrical resistivity than Pb and, therefore, electrons are transported preferentially in the Pb matrix whilst the electrons that are generated from the catalytic O_2 evolution on MnO_2 also have to pass through the catalyst particle into the Pb matrix, (ii) unequal distribution of protons that are formed during reaction (1) and locally change the electrochemical reaction rate, and/or (iii) a special two-step two-material process where generation of intermediates and formation of the final product occur on different phases of the composite electrode. The growth of the gas bubbles on the MnO_2 catalyst and thereby blocking it is a thinkable option.

Composite electrodes have been reviewed by Musiani [21]. Because the investigated composite contains particles which are 45 μm or larger in diameter, it can be assumed that the different electrodes form an array of microelectrodes [22]. Because of the low surface coverage, the diffusional fields will be practically independent [22, 23], since the distance between particles (ca. 350 μm) is about 7 times the average effective particle radius and larger than the Nernst diffusion layer. Compton et al. [23–25] have successfully proven that even for overlapping diffusion layers, the consideration of the mass transport regimes is effectively described by consideration of single idealized diffusion domains, first described by Amatore et al. [26]. These domains can be individually calculated and summed up over the entire surface of the composite electrode. Consequently, the experimental investigations of individual catalyst particles will allow to a certain extend conclusions for a whole composite electrode—also for one with a higher fraction of catalyst particles [23–25].

In this paper we use scanning electrochemical microscopy (SECM) [27–33] for the characterization of the local electrochemical processes at the composite electrode. In this technique an amperometric UME acts as a sensor in electrolyte solution and is scanned across the sample. In addition, we explore how scanning probe microscopies can contribute to the clarification of mechanistic aspects at composite electrodes. Similar works have been presented on DSA/Boron doped diamond (BDD) anode materials using CAFM and SECM [34–37] and CAFM on composite materials [38]. A new methodic aspect here are SECM

investigations under conditions of high current densities at the sample. Information gained from the presented experimental results will allow us to investigate to which extent the earlier proposed local processes have an influence on the overall observed behaviour. This will rationally guide us to further development of composite electrodes for industrial applications, especially exemplified here for Zn electrowinning.

2 Experimental

2.1 Sample preparation

For the investigation, a model sample with relatively large MnO_2 particles and low MnO_2 surface coverage was chosen to facilitate the measurement. For that purpose a sieved fraction of large MnO_2 particles ($r > 45$ μm of chemically prepared manganese dioxide CMD, "Faradiser M" from Erachem Comilog Inc., Baltimore, MD, USA.) was mixed with Pb powder (200 mesh, 99.9% from Alfa Aesar, Karlsruhe, Germany) at 1% (mass/mass) and pressed into tablets. The tablet preparation method was analogous to the method found in Ref. [19]. The tablet was soldered onto a wire and polished with 0.3 μm Al_2O_3 suspension, such that the surface which had been exposed to the tool during pressing was removed. This was followed by intense rinsing to remove the Al_2O_3 suspension.

2.2 CLSM imaging

CLSM images were recorded using a Leica TCS SP2 AOBS confocal microscope (Leica Microsystems GmbH, Wetzlar, Germany) in reflection mode, utilizing an Ar/ArKr laser operating at a wavelength of 488 nm. Overviews of the specimens were received with a HC PL FLUOTAR 5.0×0.15 objective, while more detailed images were recorded using a HC PL FLUOTAR 50.0×0.8 objective (both Leica).

2.3 CAFM experiments

A powder tablet with an unsieved fraction of MnO_2 in 10% (mass/mass) sample was pressed and polished with 0.3 μm Al_2O_3 suspension and subsequently investigated by contact mode and conducting atomic force microscopy (CAFM) in air at room temperature with a Dimension 3100 stage, a NanoScope IIIa Controller, a Quadrex extension box, and a CAFM application module (all from Veeco Instruments, Santa Barbara, CA, USA). In order to facilitate the contact mode imaging, a diamond-like carbon-coated tip was used (Veeco Probes, Santa Barbara, CA, USA, nominal length 125 μm and nominal width 30 μm). It has the advantage to be wear-resistant enough to reproduce exactly the surface topography during the CAFM scan. A linear background was subtracted from the topographic images using "NanoScope" software (version 7.20R1Sr1, Veeco) for removal of sample tilt.

2.4 SECM experiments

The pressed tablet sample (1% (mass/mass) MnO_2, $r > 45$ μm) was inserted as the bottom of a home made SECM cell (ca. 100 mL volume, Fig. 1) using nail varnish for gluing and sealing. The varnish could be removed with acetone after use. The electrochemical cell was completed by a Pt mesh and a Ag/AgCl reference electrode as auxiliary and reference electrodes, respectively. All potentials are given with respect to the Ag/AgCl reference electrode. The ultramicroelectrode (UME) used as probe was produced by sealing a Pt wire (10 μm diameter; Goodfellow, Huntingdon, UK) in glass capillary and shaping the insulating sheath to a cone with a ratio RG between the radius of glass r_{glass} and the electrode radius r_T of 5.18 μm ($RG = 9.5$) according to [39]. Before use the UME was polished with 0.3 and 0.05 μm Al_2O_3 suspension, rinsed with water and cycled in 2 M sulfuric acid solution between −0.3 V and +1.7 V vs. Ag/AgCl at 250 mV/s for cleaning and activation.

The potential of tablet sample and UME was controlled by a CHI7001B bipotentiostat (CH Instruments, Austin, TX, USA). The stepper motor positioning system of the UME (Märzhäuser Wetzlar GmbH & Co. KG, Wetzlar-Steindorf, Germany) had a closed loop feedback in x and y direction [40]. For the fine positioning in z direction a piezo with 250 μm range was used (Physik Instrumente GmbH &

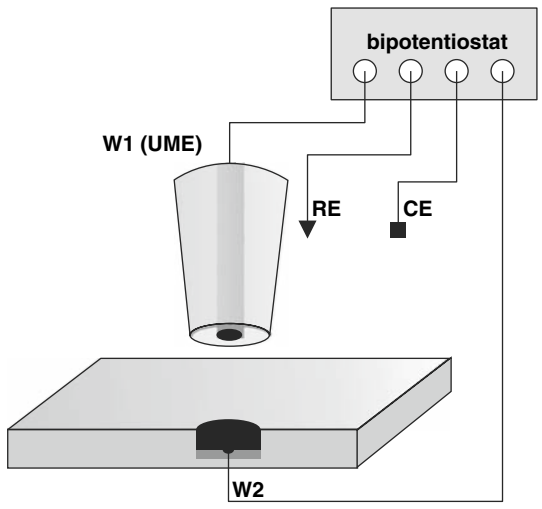

Fig. 1 Setup in the cell for SECM measurements. C, Pt mesh as counter electrode; R, Ag/AgCl reference electrode; W1, ultramicroelectrode; and W2, composite electrode

Co. KG, Karlsruhe, Germany). The tablet sample was preconditioned for 1 h at $E_S = +1.8$ V vs. Ag/AgCl. Then a potential of −0.3 V vs. Ag/AgCl was applied to the UME and held for 10 min. During this time a constant steady state current was established at the UME in the solution bulk. Afterwards, the UME was placed at a *x,y*-position from which bubbles where rising while keeping E_T constant. The approach to the surface was done while recording a substrate generation-tip collection (SG/TC) approach curve while hydrogen formation proceeded at the UME. In this way the sample evolving oxygen was found.

For the alignment of the sample tilt, the UME was first retracted by 25 μm and the sample tilt was corrected by means of a tilting stage while recording horizontal line scan. Whenever it seemed that the UME was endangered to crash into the surface, the UME was further retracted. The UME was then re-approached and retracted again to 25 μm distance. For the preparation of the *y,z* images composed of line scans at different *d,* the UME was retracted by 250 μm. The sample potential E_S was adjusted to 1.675 V vs. Ag/AgCl and hold for 10 min. Subsequently *y* line scans were conducted at *d* between 275 and 25 μm with 5 μm increments.

The *x,y* images were recorded after approach of the UME and tilt correction. Then an overview scan at $d = 125$ μm was recorded away from the region at which the approach had been performed ($E_T = -0.3$ V, $E_S = 1.7$ V, 290 × 290 μm). A spot with high activity was selected for a more detailed imaging at lower translation speed. Three images where recorded for *x,y* and *x,z* images at E_T equal to −0.3 V, −0.05 V and +1.1 V in order to detect H^+, O_2 and H_2O_2, respectively.

All recorded images were plotted using the home-written software MIRA (G. Wittstock, University of Oldenburg, Germany) [41]. For fitting the *YZ* data to an analytical expression (Eq. 6, adapted after [42] the Microsoft Excel (Microsoft, Redmond, USA) solver was used.

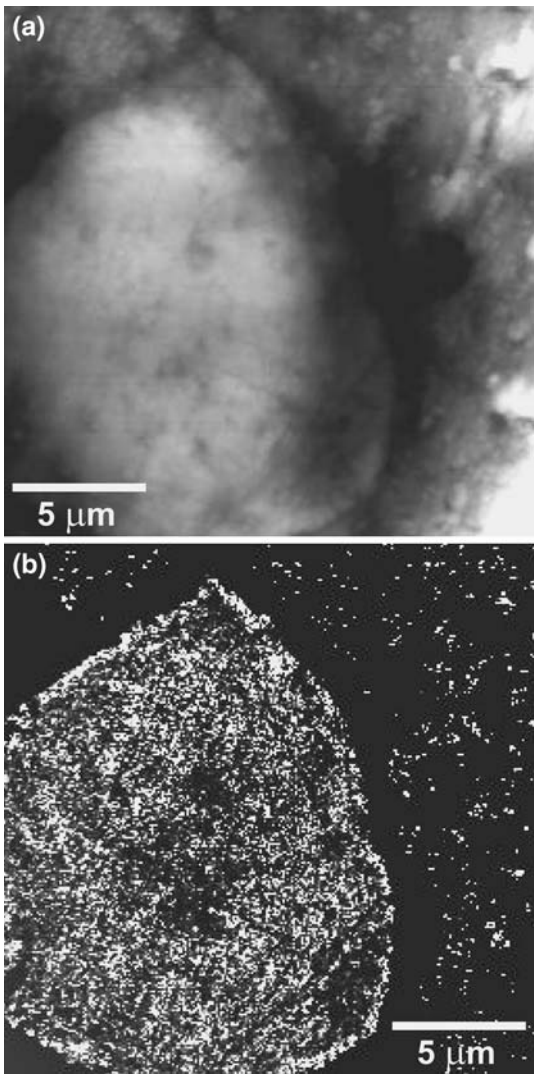

Fig. 2 20 × 20 μm AFM contact mode image (**a**, $\Delta h = 600$ nm, brighter values reflect larger heights). The simultaneously recorded CAFM image (**b**, $\Delta i = 30$ pA, $E = +500$ mV with the sample being positive to the tip) is represented in grey scale, brighter spots identifying higher currents through the DLC tip

3 Results and discussion

3.1 Topography and local conductivity of the composite electrodes

Figure 2 shows a representative section of the composite electrode as contact mode AFM image (Fig. 2a) and as conducting atomic force microscopic (CAFM) [34, 38, 43, 44] image (Fig. 2b). The electrodes were prepared from a MnO_2 particle fraction small enough to be conveniently imaged within one image frame and the *z* movement range of the AFM scanner.

The protruding area in Fig. 2a represents a MnO_2 particle. Since MnO_2 is harder than the Pb matrix, it is impossible to decrease the roughness by further polishing. Therefore, tablets were used without further treatment in scanning electrochemical microscopy experiments (vide infra). The CAFM image recorded simultaneously is shown in Fig. 2b. The potential ($\Delta E = +500$ mV sample against tip) was chosen to be similar to the situation during an anodic reaction at the composite electrode. The interpretation of the CAFM image must consider that diamond-like carbon (DLC) used as conducting coating of the AFM tip has semiconducting properties that only allow a qualitative interpretation of the image. The bulk conductivity of MnO_2 is much less then Pb. However, apart from scattering, it can be seen in Fig. 2b that the current is increased at the MnO_2 catalyst area, while less current flows across the DLC–Pb

interface. This unexpected observation can be due to passive layers on the Pb matrix or the contact of the semiconducting DLC and lead oxide layer. Nevertheless, the boundary between the MnO_2 catalyst and the Pb matrix exhibits clearly the largest currents. The reason why a higher current is passing through the boundary is probably very complex, also due to the DLC material used as AFM tip material. For a proper analysis the semiconducting properties of all materials involved and the energy levels of MnO_2, Pb and DLC have to be considered. This, however, goes far beyond the scope of this investigation.

One reasonable explanation would be the following: The DLC tip-Pb contact could be in reverse bias, such that no current flows when the DLC tip is in contact with the Pb. When the tip is located at the MnO_2 area the current has to pass also over the Pb/MnO_2 junction which could be a negatively biased Schottky junction (working function lead ca. 4.1 eV [45], MnO_2 with a Fermi level of 6–6.5 eV [46]). At the boundary however, between both materials of the composite, it could be that a 100–200 nm broad space charge layer (compare to Fig. 2b). The space charge layer is usually characterised by a high density of minority charge carriers (holes in the *n*-type MnO_2) and surface states through which the electrons might be easily transferred into the composite.

A situation where the composite is in contact with the electrolyte can be similar. MnO_2, as a *n*-type conductor, would normally be blocking in anodic direction. At the boundary however, the minority charge carriers (holes) of the space charge layer might allow to transfer electrons from the electrolyte into the electrode. This would restrict the anodic current to a very thin stripe at the matrix catalyst boundary, which would meet the assumptions of the model proposed earlier [19].

A larger overview of the sample was obtained by CLSM in the reflection mode (Fig. 3). One can see that the catalyst particle comprise only a small fraction of the total surface area. For the preparation of samples for SECM 1% (mass/mass) MnO_2 was used.

3.2 SECM measurements of diffusion layers in the *y,z* plane

The substrate-generation tip-collection (SG/TC) mode was used to measure the concentration of electrochemically active species near the oxygen evolving composite electrode. For the measurement of the hydrogen peroxide intermediate a redox competition has to be taken into consideration because both the reaction at the catalyst and the reaction at the tip could compete with each other. In order to enable the observation of reactions at an individual particle, large MnO_2 particles ($r > 45$ μm) were sieved out and processed to a sample with a low surface fraction (1% (mass/mass)). Realizing a large particle-to particle distance (here ca. 350 μm) is important in the SG/TC mode because small very active regions may prevent the detection of closely spaced regions of somewhat lower reactivity [47]. With these samples, potentially present edge effects should be more distinct and the resolution of SECM should be sufficient to resolve these at the matrix-catalyst particle boundary.

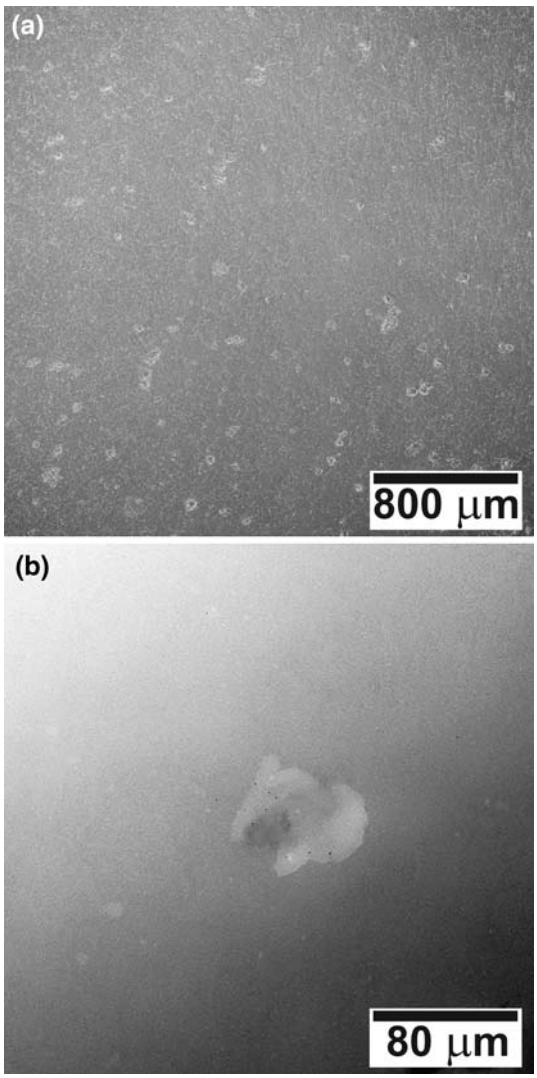

Fig. 3 CLSM topographical images of the investigated sample. **a** Overview recorded with the 5× objective; **b** image of one particle recorded with the 50× objective

A typical approach curve to the sample can be seen from Fig. 4. The sample is under potentiostatic control and produces H^+ during oxygen evolution. The Pt UME is reducing H^+ originating from the electrolyte bulk (2 M H_2SO_4) or from the reaction at the sample surface. Consequently, the H^+ reduction current i_T at the UME is increasing with decreasing distance $d > 15$ μm. At $d < 15$ μm, i_T decreases because the insulating sheath of

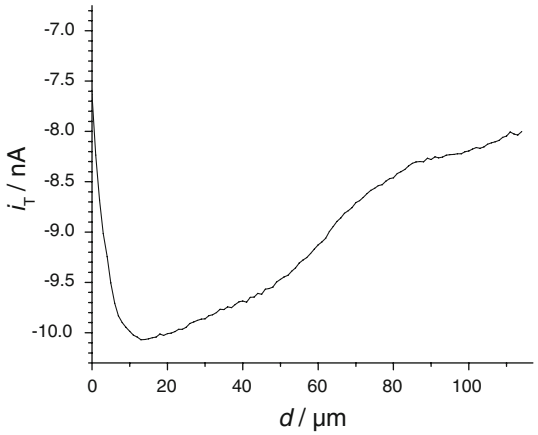

Fig. 4 Typical SECM approach curve to the composite electrode in the SG/TC mode in 2 M H_2SO_4, $E_S = +1.8$ V, $E_T = -0.3$ V (H^+ reduction), UME translation rate $v_T = 10$ µm s^{-1}

the UME shield mass transport processes to the sample region underneath the UME as well as transport from the solution bulk to the UME surface. This leads to a local pH change and decreasing reduction currents i_T at $d < 15$ µm. Such effects are commonly observed in SG/TC experiments [48].

Images of local product concentration during oxygen evolution at the sample was obtained by recording series of horizontal scans at different distances (*y*,*d* images, Fig. 6a) with different potentials E_T applied to the probe: −0.3 V for the detection of protons at the UME (Eq. 3), −0.05 V for the reduction of oxygen (Eq. 4), and +1.1 V for detection of H_2O_2 (Eq. 5). The microelectrode potentials were chosen from cyclic voltammograms of the microelectrodes positioned in the bulk solution, similar to the approach followed in Ref. [49].

$$2H^+ + 2e^- \rightarrow H_2; E_T = -0.3 \text{ V vs. Ag/AgCl} \quad (3)$$

$$O_2 + 4H^+ + 4e^- \rightarrow 2H_2O; E_T = -0.05 \text{ V vs. Ag/AgCl} \quad (4)$$

$$H_2O_2 \rightarrow O_2 + 2H^+ + 2e^-; E_T = 1.1 \text{ V vs. Ag/AgCl} \quad (5)$$

Figure 5a shows the difference between N_2-saturated and O_2-saturated solutions which were achieved by purging a cell with the respective gases under slight overpressure. Oxygen reduction starts at around 0.8 V. Because the difference between N_2 saturated and O_2 saturated solutions was biggest at ca. −0.05 V we chose this potential for the oxygen detection at the UME.

On the first view, it does not seem possible to separate hydrogen evolution and oxygen reduction reaction at the microelectrode, when a potential of $E_T = -0.3$ V is chosen. However, considering the very small concentration of

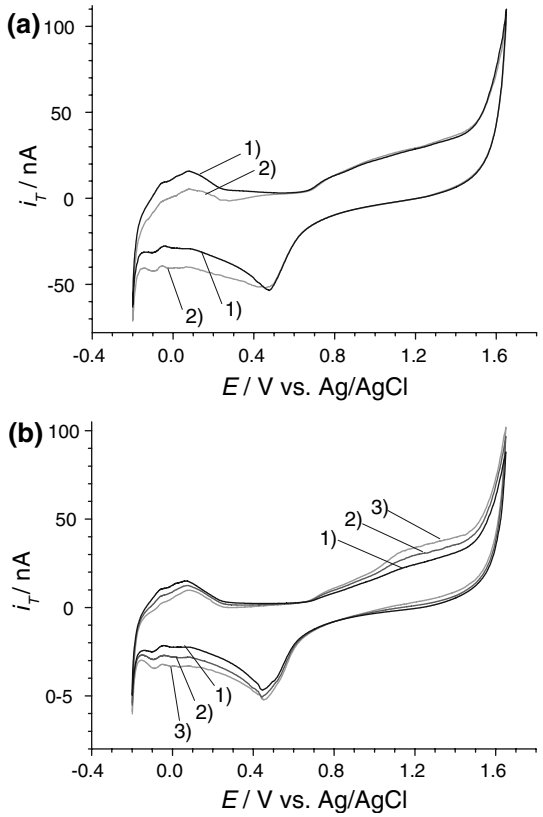

Fig. 5 Cyclic voltammogramms recorded at a Pt UME at 0.1 V s^{-1} in 2 M H_2SO_4. **a** N_2-saturated solution (*curve 1*) and O_2-saturated solution (*curve 2*); **b** N_2-saturated solution with additions of H_2O_2, $[H_2O_2] = 0$, 1 mM and 2 mM

dissolved oxygen compared to the proton concentration, this distinction is possible. The oxygen concentration in 0.1 M H_2SO_4 is about 0.27 mmol L^{-1} [50, 51] and its contribution to the current can be considered to be negligibly small at −0.3 V.

The detection potential for H_2O_2 at the UME was determined by a series of cyclic voltammogramms at increasing H_2O_2 concentrations (Fig. 5b). We selected the oxidation reaction of H_2O_2 (Eq. 5) which starts at ca. 0.8 V and reaches its maximum sensitivity at about 1.1 V, which was used as the UME potential to sense H_2O_2.

In order to determine concentration profiles of the H^+, O_2 and H_2O_2, series of horizontal scans at different *d* (*y*,*d* images, schematic in Fig. 6a) were recorded at $E_T = -0.3$ V, −0.05 V and 1.1 V. The scatter of the data in Fig. 6b–c is due to the convection caused by the macroscopically visible formation of gas bubbles during oxygen evolution at the sample. However, relative concentrations within the diffusion layer can still be evaluated. Both, the local proton concentration (Fig. 6b) and the local oxygen concentration (Fig. 6c) increase substantially towards the

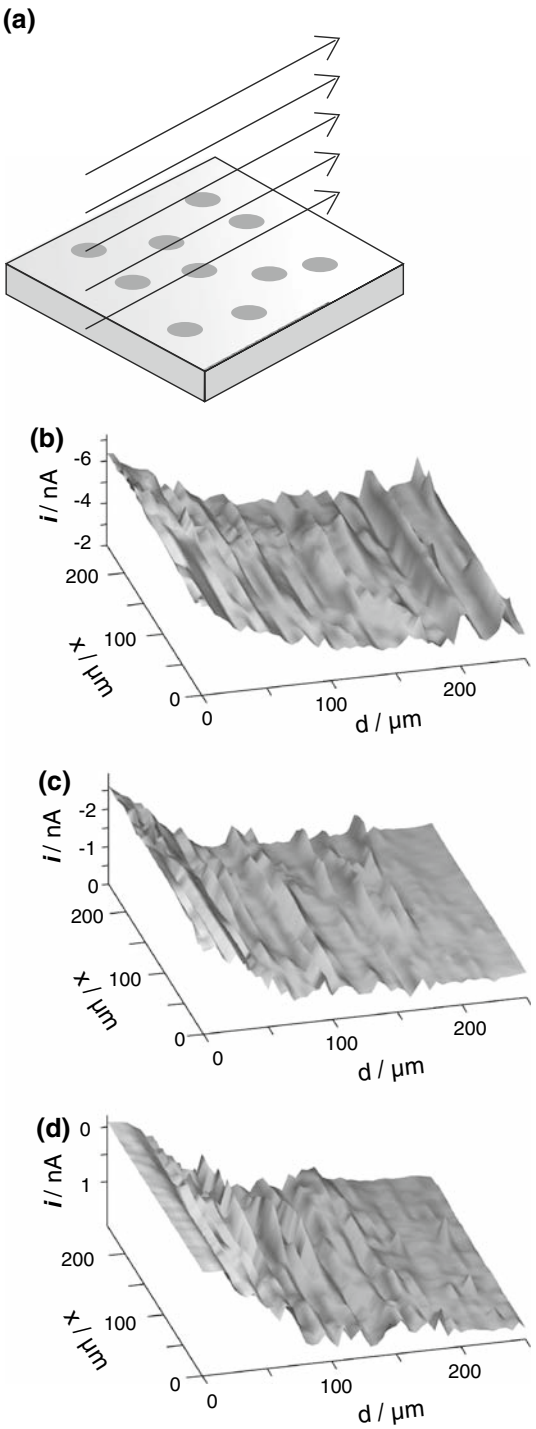

Fig. 6 SECM SG/TC mode images of the composite electrode during oxygen evolution within a plane vertical to the composite electrode (*y*,*z*). **a** Schematic representation of the recorded line scans; **b** H^+ concentration; $E_T = -0.3$ V, $E_S = +1.675$ V, $v_T = 23$ µm s^{-1}; **c** O_2 concentration; $E_T = -0.05$ V, $E_S = +1.675$ V, $v_T = 15$ µm s^{-1}; **d** H_2O_2 concentration $E_T = 1.1$ V, $E_S = +1.675$ V, $v_T = 15$ µm s^{-1}

electrode surface. It can be expected that such an increase affects the reaction kinetics at the sample by a concentration overvoltage. The image taken at $E_T = 1.1$ V shows that the H_2O_2 is involved as an intermediate in the electrode reaction (Fig. 6d). Just recently H_2O_2 generated from oxygen reduction on Pt and Pd/Co in acidic media has been detected under similar conditions at the same UME potential [49, 52].

In order to evaluate key properties of the involved species more in detail, data for each d were averaged from the recordings at that d and all lateral positions y within 245 µm. Since the measured tip current scales linearly with the surrounding concentration, a proportionality factor k was introduced which transferred measured tip current directly into concentration values. If the bulk concentration c_b of the active species is known, this constant is well defined by tip currents far away from the sample surface which directly relate to the bulk concentration. For unknown bulk concentrations it has to be evaluated.

The data related to the averaged concentration could be fitted to a theoretical expression of semi-infinite linear diffusion at constant sample current (Eq. 6 adapted after [42]; for meaning of symbols see text below):

$$c(d,t) = c_b + \frac{j_{avg}}{nFD}\left[2\left(\frac{Dt_G}{\pi}\right)^{0.5}\exp\left(-\frac{d^2}{4Dt_G}\right) - d\cdot\operatorname{erfc}\left(\frac{d}{2(Dt_G)^{0.5}}\right)\right] \quad (6)$$

with n the number of exchanged electrons, F the Faraday constant, D the diffusion coefficient, and t the time after the start of the experiment. Despite our experiments are done potentiostatically, this formula can be applied for a steady state system. The steady state is reached in this experiment because the gas evolution causes convection preventing a further outspread of the Nernst diffusion layer. Using the galvanostatic transition time t_G in Eq. 6 as adjustable parameter allows to estimate how long it approximately takes until the steady state Nernst diffusion layer of the electrochemical active species under investigation has built up. As other fitting parameter the average current density j_{avg} can be obtained, which is the average current density that generates the species at the surface of the sample (averaged over all y positions with fixed x). Also the bulk concentration c_b, if unknown, can be fitted.

By extrapolation, the surface concentration $c_s = c$ ($d = 0$) can be obtained, which can be also expressed as a normalized surface concentration ($C_s = c_s/c_b$). The thickness δ of the Nernst diffusion layer $d = \delta$ is taken as the intersection of the linear fit $c = f(d)$ close to the electrode with the line $c = c_b$ and characterizes the influence of the convection.

For the fitting of the proton concentration (Fig. 7b) the absence of a supporting electrolyte must be considered. Therefore, the diffusion and migration of protons is

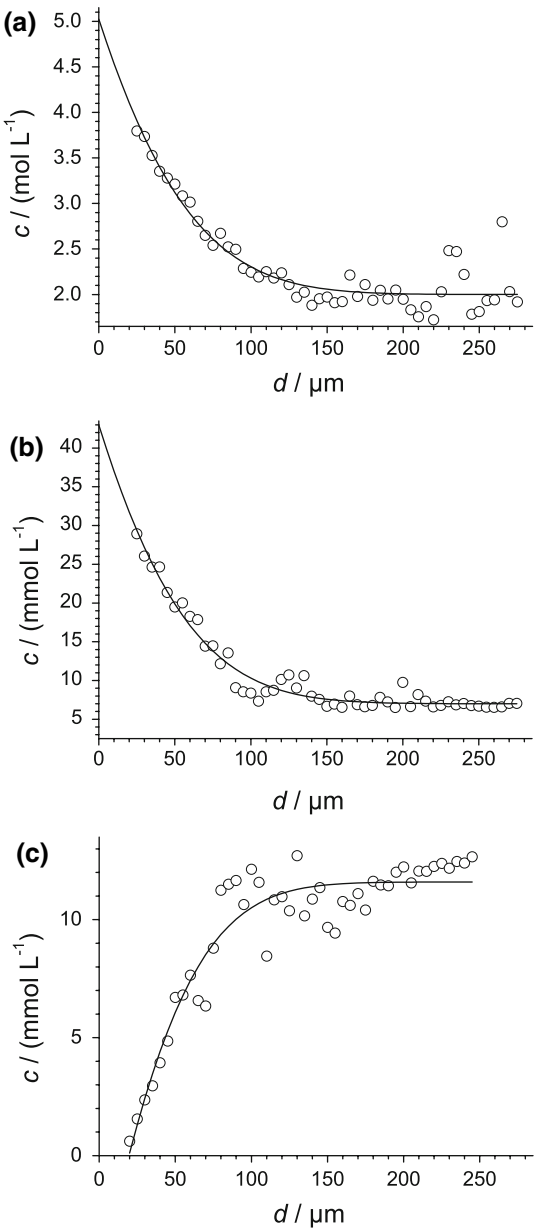

Fig. 7 Fitting results for the *yz* images in Fig. 6 averaged for each working distance **a** H^+ concentration; **b** O_2 concentration; **c** H_2O_2 concentration

coupled to that of hydrogensulphate ions. Due to the electroneutrality requirement both concentrations have to be equal and instead of two different diffusion constants for each ion the effective salt diffusion coefficient for sulphuric acid ($D \approx 2.2 \times 10^{-5}$ cm^2 s^{-1} [53]) can be used. This coupled diffusion process is much slower than the single ion diffusion coefficient for protons in a supporting electrolyte solution. The bulk concentration of sulphuric acid ($c_b = 2$ M) was left constant whilst all other parameters D, t_G, j_{avg} were fitted.

For oxygen concentration profiles (Fig. 7c) the literature diffusion coefficient ($D_{O_2} = 1.9 \times 10^{-5}$ cm^2 s^{-1} [54]) was used, but the bulk concentration under the condition of the oxygen evolution was unknown. Therefore additionally to j_{avg}, t_G and c_b also the proportionality factor had to be fitted. Including also the diffusion coefficient as a fitting variable leads to results that were very dependent on the starting values, which was not the case for the fixed literature diffusion coefficient.

For hydrogen peroxide (Fig. 7d) the fitting was not possible within the original z coordinate system (otherwise negative concentrations would have resulted). The fitting was done for $d' = d - 20$ µm. A solution (which was not dependent on the starting values) was obtained by fitting all parameters (D, j_{avg}, t_G and c_b), including the proportionality factor k.

The results of the fits are summarized in Table 1. Equation 6 can be used quite successfully to describe the data as we observe a good description of the experimental data by the theoretical function. For both protons (or sulphuric acid) and hydrogen peroxide, diffusion coefficients similar to the literature values ($D_{H_2O_2} = 1.8 \times 10^{-5}$ cm^2 s^{-1}, compare to [49]) were obtained and all fitted parameters were in reasonable ranges.

The fitted average current densities for oxygen and protons generation are both larger than the macroscopic current density 0.0075 A cm^{-2} obtained by dividing the sample current i_S by the geometric area of the sample. For oxygen it can be assumed that most of it is removed via gas bubbles and only minor parts diffuse away, thus its actual average generation current density is expected to be larger than the fitted value. For proton generation the fitted value should reflect more or less correctly the current densities at the underlying sample, which indicates (if all active areas had that same activity) that less than 1% of the surface are active. This is the same order of magnitude as the catalyst fraction that was used (1% in weight).

Oxygen would be present in the solution in supersaturation (above the solubility limit of ca. 1 mM [50, 51]). This could happen if the heterogeneous gas bubble formation process is too slow to sufficiently remove oxygen and the homogenous nucleation rate is strongly impeded in the bulk solution. Hydrogen peroxide can be described to be present in considerable amounts.

The averaging decreased the noise in the current data to an acceptable value that is worth noting as we expect a turbulent flow caused by the rising oxygen bubbles. Due to the considerable convection, the Nernst diffusion layer is small and consistent in the three independent experiments [$\delta = (60–75)$ µm]. Although bubbles could not be seen or detected, it is nevertheless possible to assess the influence of convection with its key variable δ. The Nernst diffusion layer thickness is very small, but such small diffusion layers at macroscopic electrodes have been measured before for the oxygen evolution reaction [55]. SECM also appears to

Table 1 Parameters used in fitting experimental results to Eq. 6

Detected species	Fitting parameters					Calculated values		
	$D/(\mathrm{cm^2 s^{-1}})$	t_G/s	$j_{avg}/(\mathrm{A\ cm^{-2}})$	c_b/M	$k/(\mathrm{nA\ M^{-1}})$	c_s/M	C_s	δ/μm
H^+	$\mathbf{2.3 \times 10^{-5}}$	**1.18**	**1.14**	2	−1.73	5.1	2.11	65
O_2	1.9×10^{-5}	**1.34**	$\mathbf{4.6 \times 10^{-2}}$	$\mathbf{7.0 \times 10^{-3}}$	**90.2**	3.2×10^{-2}	6.14	64
H_2O_2	$\mathbf{1.8 \times 10^{-5}}$	**0.92**	$\mathbf{8.7 \times 10^{-3}}$	$\mathbf{1.2 \times 10^{-2}}$	**162**	(1.1×10^{-4})	(0.01)	73 (53)

Values in bold are fitted. Values in brackets are calculated results for $d_0 = 20$ μm

be a good method to study convection at gas evolving electrodes, i.e. under condition of much stronger convection, because it can measure the thickness of the Nernst diffusion layer. There are not many reports on SECM in media with turbulent convection. Previous SECM work in systems with rising gas bubbles in the context of oxygen consuming electrodes produced qualitative images [56]. SECM has been used before to study the influence of natural convection on currents at microelectrodes [57–59]. The possibility to measure the Nernst diffusion layer thickness quantitatively in media heavily influenced by convection is new and had been difficult earlier.

The images in Fig. 7b and c show substantial concentration gradients between the bulk solution and the electrode surface for H^+ and O_2. The oxidation of water (Eq. 1) is an irreversible reaction and thus on the first sight it should not depend on proton and oxygen concentration. However, the reaction involves several adsorbed surface intermediates which are connected to the local solute concentrations of H^+ and O_2 by equilibrium reactions [60]. To understand why c_{H+} and c_{O_2} influence the reaction, the entire oxygen evolution mechanism has to be considered. As an example we take the electrochemical oxide path mechanism at a surface site S [60]:

$$S + H_2O \rightarrow S\text{-}OH + H^+ + e^- \quad (7)$$

$$S\text{-}OH \rightarrow S\text{-}O + H^+ + e^- \quad (8)$$

$$2S\text{-}O \rightarrow O_2 + 2S \quad (9)$$

If the first step is rate-determining, the reaction requires next to water free active surface sites to which water can be adsorbed. Free active surface sites are released in the last step. Although the first step is rate determining, the rate expressions of the following steps cannot anymore be neglected. If we assume steps (8) and (9) to be in equilibrium, then backward reactions of these steps also take place and the recovery of active sites is slowed down by increased H^+ and O_2 solution concentration at the surface.

Taking the negative reaction order of H^+ and O_2 for granted, the H^+ and O_2 concentration overvoltage can be derived from the difference of two Tafel expressions (Eq. 10). One is derived for the measured solute concentration close to the surface and the other is setup for the bulk concentration. Equation 10 describes the voltage difference between the real system, where mass transport plays a role, and a system where mass transport influence is virtually absent.

$$\eta_c = b[\log j(c_b) - \log (c_s)] = b \log \frac{j(c_b)}{(c_s)} = b \log \left(\frac{nFk}{nFk} \frac{c_b^a}{c_s^a} \right) = ab \log \frac{c_b}{c_s} = -ab \log C_s \quad (10)$$

η_c, b and j describe the concentration overvoltage, Tafel slope and the current density. k and a are electrochemical rate constants and reaction order. For the investigated reaction, we used $b = 120$ mV/dec [19], assumed $a = -1$ in agreement with earlier publications [61] and took the experimental result of $C_s = 2.11$ for H^+ (Table 1). This results in a proton concentration overvoltage of $\eta_c = 39$ mV. For oxygen ($C_s = 6.14$, $b = 120$ mV/dec, $a = -0.5$ or -0.025) η_c equals 47 mV or 24 mV. Both values are of considerable size meaning that a maximum improvement of 39 mV for H^+ plus a 47 mV improvement for O_2 are thinkable when the assumed reaction orders represent the actual reaction kinetics. Whether spherical diffusion is powerful enough to obtain significantly improved performance with smaller catalyst particles (e.g. 20 μm [19]), cannot be said at this point as it depends on too many variables such as composite electrode properties and kinetics [26]).

3.3 SECM images in *x,y* direction

After approach and tilt correction described in the Experimental section, an survey image parallel to the surface (*x,y* plane, scheme in Fig. 8a) was recorded. The survey scan at $d = 125$ μm is shown in Fig. 8b. Smaller d were not useful due to the protruding catalyst particles (Figs. 2a and 3). A spot with high activity indicated by a white rectangle in Fig. 8b was chosen for a more detailed investigation at lower translation rate. The results are shown in Fig. 9a–c for the detection of H^+, O_2 and H_2O_2, respectively. In order to aid comparisons, the gray scales were selected such that bright colours represent higher concentrations in Figs. 8b and 9. All images show that the concentration distribution for all species is inhomogeneous along the sample surface

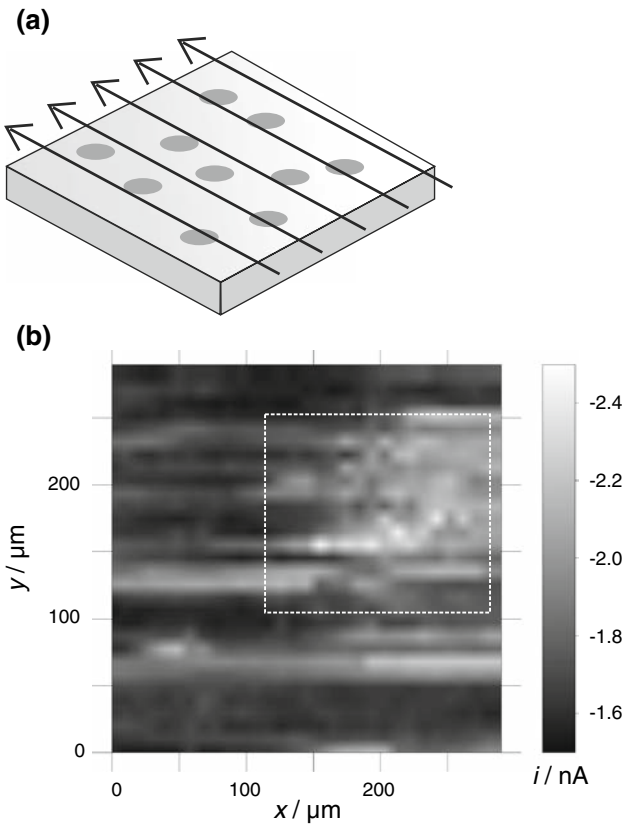

Fig. 8 SECM SG/TC mode images of the composite electrode during oxygen evolution within a plane parallel to the composite electrode (*x,y*); **a** Schematic representation of the line scans; **b** experimental data for a frame of 290 × 290 µm at $d = 125$ µm. $E_S = 1.7$ V, $E_T = -0.3$ V, $v_T = 9$ µm s^{-1}. The white rectangle shows the area inspected in Fig. 9

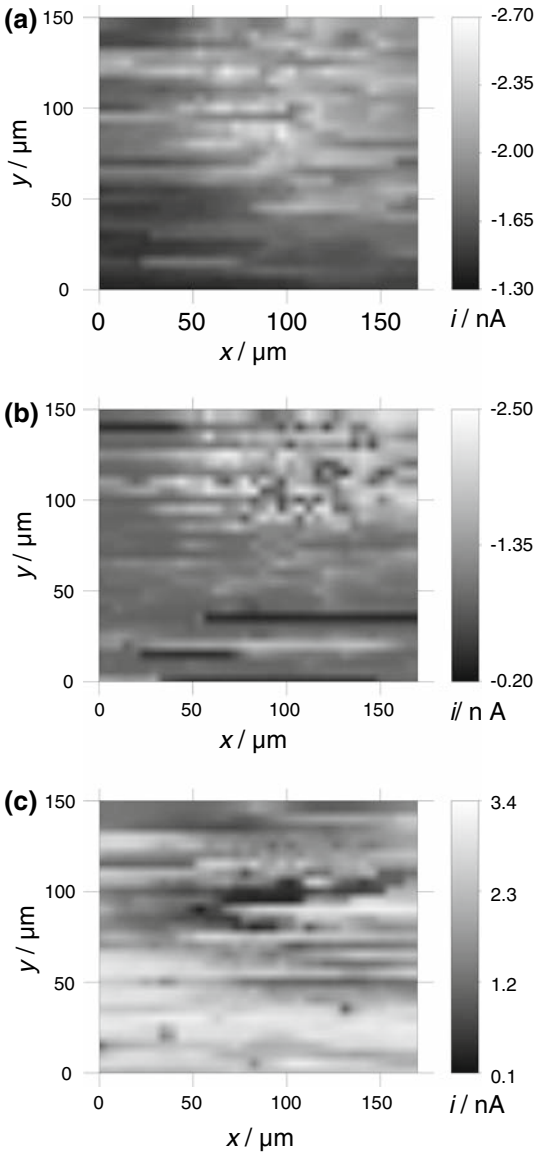

Fig. 9 SECM SG/TC mode images (170 × 150 µm) of the composite electrode during oxygen evolution within a plane parallel to the composite electrode (*x,y*); $d = 125$ µm, $v_T = 23$ µm s^{-1} (**a**) and 10 µm s^{-1} (**b**, **c**), $E_S = 1.7$ V; **a** $E_T = -0.3$ V (H^+); **b** $E_T = -0.05$ V (O_2); **c** $E_T = 1.1$ V (H_2O_2)

even at $d = 125$ µm. Proton concentration and oxygen concentration is increased in the upper right region while hydrogen peroxide seems to be consumed in this area. This would be in accordance with Eq. 5. The remaining part of the image frame seems to be inactive for proton and oxygen generation, but an increased H_2O_2 concentration is found, which is possibly generated at that area.

An interpretation of Fig. 9 must consider the influence of topography and local reactivity on SECM images. Since the catalyst particles protrude from the matrix (Figs. 2a and 3), both distance and local reactivity change within the image frame. It should be noted that shear-force distance control is not applicable to this sample due to the severe interference of local convection with the mechanical shear force detection. Therefore, the interpretation of the role of H_2O_2, which seems to be consumed at the electrode (*y,d* image, Figs. 6d and 7c) is impossible in a consistent way. On the one hand its lateral concentration distribution follows opposite trends than those of H^+ and O_2. (*x,y* scans, Figs. 6b–d and 9a–c) and the extension of the area with decreased currents for H_2O_2 oxidation and increased oxygen and proton reduction agrees with the mean size of the used catalyst particles. On the other hand, it cannot be clearly said whether the decreased currents in the upper right part of Fig. 9c could be due to shielding of H_2O_2 diffusion from the solution bulk by the protruding catalyst particle or whether an increased H_2O_2 consumption is observed at the MnO_2 catalyst particle or both. From the CLSM measurements (Fig. 3) it is known that the particles protrude from the surface of the composite electrode, thus a topographical contrast is likely.

Possible reactions of hydrogen peroxide at the composite electrode are:

$$2H_2O_2 \rightarrow O_2 + 2H_2O \quad (11)$$

$$H_2O_2 \rightarrow O_2 + 2H^+ + 2e^-; E^\circ = 0.70 \text{ V vs. SHE} \quad (12)$$

If it would be, however, exclusively be a topographical contrast this would also mean that the MnO_2 area of the electrode would not be interacting with H_2O_2 which it expected due to its ability to catalyse H_2O_2 decomposition reaction to oxygen and water (11). In addition, also oxidation of H_2O_2 to oxygen and protons (12) might be possible under electrochemical conditions. Reaction (12) could be difficult if a blocking *n*-type MnO_2-electrolyte contact is present or an area is not easily supplied with current (compare to CAFM results in Fig. 2b). Because a H_2O_2 reaction would be logical at the MnO_2 catalyst we should take into consideration that we have both a topographical contrast and a reaction of H_2O_2.

Another important issue is the origin of H_2O_2. Since it was not deliberately added to the solution, it could be generated at the Pt auxiliary electrode by reduction of oxygen. This is, however, very unrealistic because also Pt is a good catalysts for H_2O_2 reduction and could not build up such high bulk concentrations as found here.

Although we were not able to show that H_2O_2 is generated at some part of the electrode (only its consumption was clearly demonstrated), there could be also the possibility that there are regions at the electrode where H_2O_2 is generated (for example at the Pb matrix). This would be interesting to know, since it was earlier identified as one possible reason why the boundaries at composite electrodes are of particular importance as described by the model developed earlier. In such a scenario generating and consuming areas of H_2O_2 would be very close to each other and pronounced edge effects would be expected.

There is no evidence for adhering gas bubbles on MnO_2 (compare to Fig. 2b in Ref. [62]). They would be clearly visible in all images in Figs. 8 and 9.

4 Conclusions

Scanning probe microscopic techniques could show local electric/electronic, topographic and electrochemical properties of model composite electrodes prepared to mimic important properties of new technologically electrodes produced by Outotec by spraying catalytically active MnO_2 particles coating onto existing Pb anodes for metal electrowinning. CAFM pictures in air showed that the boundary region between the MnO_2 catalyst and the Pb matrix has special properties.

Local electrochemical measurements using the SG/TC mode of SECM proved that three major species seem to be involved in the electrode reaction: H^+, O_2 and the intermediate H_2O_2. For all of the species mass transport was played a significant role because the concentrations near the electrode deviated from the bulk concentration. Comparison of the experimental data for different working distances allowed a comparison to quantitative models despite the substantial interference of convection due to raising O_2 gas bubbles. From fitting the experimental results to the theoretical expression, parameters such as average current density at the underlying sample, transition times for steady state, bulk concentration and concentration at the surface were obtained. They allowed an estimation of the concentration overvoltage. For reasonable reaction orders with respect to H^+ and O_2 it amounts to about 40–50 mV for each reaction.

It is worth emphasizing that quantitative SECM experiments in media with turbulent convection open new possibilities for investigation of technologically important electrodes. The investigated samples are rough and could not been flattened by polishing procedures. Therefore, further interpretation of SECM images must be done with some care, as the images will represent an overlap of topographic and reactivity effects. From the measurements it seems likely that the consumption of H_2O_2 occurs on the catalyst particle either by disproportionation or by oxidation to oxygen.

Three of the possible physical reasons for an inverse proportionality between the macroscopic current density and the mean MnO_2 particle radius which has been observed experimentally [19], have been investigated and all of them were found to be realistic reasons. Adhering gas bubbles however, which one would expect to be visible in SECM could not be seen.

Acknowledgments The work has been partially supported by Deutsche Forschungsgemeinschaft (DFG, grant Wi 1617/8). Sönke Schmachtel wishes to acknowledge financial support by Outokumpu foundation and ESPOM graduate school, and Outotec for covering material costs.

References

1. Aromaa J, Evans JW (2007) In: Bard AJ, Stratmann M, Macdonald D et al (eds) Encyclopedia of electrochemistry, vol 5. Wiley-VCH, Weinheim
2. Moats MS (2008) JOM 60:46
3. Beer HB (1961) German patent 1115721
4. Beer HB (1966) Dutch patent 6606302
5. Beer HB (1972) US patent 6800834
6. Beer HB (1976) US patent reissue 28820
7. Beer HB, Hinden JM (1981) European patent 27051
8. Beer HB, Hinden JM (1982) European patent 46447
9. Hinden JM, Beer HB (1982) European patent 46449
10. Chandler GK, Genders JD, Pletcher D (1997) Platinum Met Rev 41:54
11. Hayfield PCS (1998) Platinum Met Rev 42:27
12. Hayfield PCS (1998) Platinum Met Rev 42:46
13. Thonstad J (1998) Elektrolyseprosesser. Norwegian University of Science and Technology, Trondheim

14. Bestetti M, Ducati U, Kelsall GH et al (2001) Can Metall Q 40:451
15. Åkre T (2008) Electrowinning of cobalt from chloride solutions—anodic deposition of cobalt oxide on DSA. Doctoral thesis, Norwegian University of Science and Technology, Trondheim
16. Veräjänkorva S (2005) Thermal spraying of catalytic materials. Masters Thesis, Tampere University of Technology, Tampere
17. Gaertner F, Stoltenhoff T, Schmidt T et al (2006) J Therm Spray Technol 15:223
18. Barker MH, Hyvaerinen O, Osara K (2007) International patent 2007045716
19. Schmachtel S, Toiminen M, Kontturi K et al (2009) J Appl Electrochem 39 (in press)
20. Schmachtel S (2004) Development of acid resistant coatings for oxygen evolving anodes for the electrowinning of zinc or copper. Diploma Thesis, Christian-Albrechts-Universität, Kiel
21. Musiani M, Guerriero P (1998) Electrochim Acta 44:1499
22. Stulik K, Amatore C, Holub K et al (2000) Pure Appl Chem 72:1483
23. Davies TJ, Compton RG (2005) J Electroanal Chem 585:63
24. Davies TJ, Banks CE, Compton RG (2005) J Solid State Electrochem 9:797
25. Ordeig O, del Campo J, Munoz FX et al (2007) Electroanalysis 19:1973
26. Amatore C, Saveant JM, Tessier D (1983) J Electroanal Chem 147:39
27. Pust SE, Maier W, Wittstock G (2008) Z Phys Chem 222:1463
28. Wittstock G, Burchardt M, Pust SE et al (2007) Angew Chem Int Ed 46:1584
29. Lu X, Wang Q, Liu X (2007) Anal Chim Acta 601:10
30. Sun P, Laforge FO, Mirkin MV (2007) Phys Chem Chem Phys 9:802
31. Edwards MA, Martin S, Whitworth AL et al (2006) Physiol Meas 27:R63
32. Amemiya S, Guo J, Xiong H et al (2006) Anal Bioanal Chem 386:458
33. Gyurcsanyi RE, Jagerszki G, Kiss G et al (2004) Bioelectrochemistry 63:207
34. Macpherson JV, Gueneau de Mussy J-P, Delplancke J-L (2001) Electrochem Solid State Lett 4:E33
35. Macpherson JV, Gueneau de Mussy J-P, Delplancke J-L (2002) J Electrochem Soc 149:B306
36. Gueneau de Mussy J-P, Macpherson JV, Delplancke J-L (2003) Electrochim Acta 48:1131
37. Wilson NR, Clewes SL, Newton ME et al (2006) J Phys Chem B 110:5639
38. O'Hare D, Macpherson JV, Willows A (2002) Electrochem Commun 4:245
39. Kranz C, Ludwig M, Gaub HE et al (1995) Adv Mater 7:38
40. Nunes Kirchner C, Hallmeier KH, Szargan R et al (2007) Electroanalysis 19:1023
41. Wittstock G, Asmus T, Wilhelm T (2000) Fresenius J Anal Chem 367:346
42. Bard AJ, Faulkner LR (2001) Electrochemical methods: fundamentals and applications, 2nd edn. John Wiley & Sons, New York
43. O'Shea SJ, Atta RM, Welland ME (1995) Rev Sci Instrum 66:2508
44. Trenkler T, Hantschel T, Stephenson R et al (2000) J Vac Sci Technol B 18:418
45. Trasatti S (2005) Russ J Electrochem 41:1255
46. Xu Y, Schoonen MAA (2000) Am Mineral 85:543
47. Sklyar O, Träuble M, Zhao C et al (2006) J Phys Chem B 110:15869
48. Horrocks BR, Schmidtke D, Heller A et al (1993) Anal Chem 65:3605
49. Shen Y, Träuble M, Wittstock G (2008) Anal Chem 80:750
50. Gubbins KE, Walker RD Jr (1965) J Electrochem Soc 112:469
51. Carano M, Holt KB, Bard AJ (2003) Anal Chem 75:5071
52. Shen Y, Träuble M, Wittstock G (2008) Phys Chem Chem Phys 10:3635
53. Lobo VMM (1989) Handbook of electrolyte solutions, part A. Elsevier, Amsterdam
54. Juermann G, Schiffrin DJ, Tammeveski K (2007) Electrochim Acta 53:390
55. Nefedov VG, Artyushenko OA, Kashevarova EV (2006) Russ J Electrochem 42:638
56. Karnicka K, Eckhard K, Guschin DA et al (2007) Electrochem Commun 9:1998
57. Heinze J (1981) J Electroanal Chem 124:73
58. Amatore C, Szunerits S, Thouin L et al (2001) J Electroanal Chem 500:62
59. Pohl P, Saparov SM, Antonenko YN (1998) Biophys J 75:1403
60. Trasatti S, Lodi G (1980/81) In: Trasatti S (ed) Electrodes of conductive metallic oxides, B, Elsevier, Amsterdam
61. Morita M, Iwakura C, Tamura H (1977) Electrochim Acta 22:325
62. Wilhelm T, Wittstock G (2000) Mikrochim Acta 133:1